SAND2000-2508J

Effect of Computational Domain Size on the Mathematical Modeling of Transport Processes During Directional Solidification.

C. FRUEH, D.R. POIRIER AND S.D. FELICELLI[1]

Using a finite element simulator, a directionally solidified hypoeutectic Pb-Sn alloy was modeled to determine the effect of the height of the overlying liquid on convective transport and macrosegregation. It was determined that, while the strength of the convection in the overlying liquid depends on the square root of its height, one need not model the entire domain to predict freckling. Furthermore, the assumption of a constant thermal gradient in the liquid causes the predicted convection to be somewhat weaker than the convection in a temperature field used in directional solidification processing.

I. INTRODUCTION

The present study is concerned with obtaining an improved understanding of the transport phenomena in the documented experiments of Tewari and Shah[1], who directionally solidified Pb-Sn alloys under rather steep thermal gradients of approximately 70 to 100 $K \cdot cm^{-1}$. In our previous work and in that of others, the simulation of the DS process with uniform gradients has been performed. Directional solidification, however, is usually done by moving the specimen (or casting) relative to the coordinates of a furnace with a hot zone and cold zone (*i.e.*, a Bridgeman furnace); hence the liquid above the advancing solidification front has a rather steep thermal gradient near the front which drops off away from the front and approaches zero in the hot zone where the temperature is almost uniform. Therefore, the overlying liquid approximately comprises a layer with a uniform thermal gradient under a layer with an almost isospatial temperature. The closest to simulating the temperature field in DS was

---

[1] C. Frueh is a Graduate Professional Intern in the Mechanical Reliability and Melting Department at Sandia National Laboratories, Albuquerque, NM 87185. D.R. Poirier, Professor, is with The Department of Materials Science and Engineering, The University of Arizona, Tucson, AZ 85721. S.D. Felicelli, Research Scientist, is with Centro Atómico Bariloche, 8400 S.C. de Bariloche, Argentina.

DISCLAIMER

This report was prepared as an account of work sponsored by an agency of the United States Government. Neither the United States Government nor any agency thereof, nor any of their employees, make any warranty, express or implied, or assumes any legal liability or responsibility for the accuracy, completeness, or usefulness of any information, apparatus, product, or process disclosed, or represents that its use would not infringe privately owned rights. Reference herein to any specific commercial product, process, or service by trade name, trademark, manufacturer, or otherwise does not necessarily constitute or imply its endorsement, recommendation, or favoring by the United States Government or any agency thereof. The views and opinions of authors expressed herein do not necessarily state or reflect those of the United States Government or any agency thereof.

DISCLAIMER

Portions of this document may be illegible in electronic image products. Images are produced from the best available original document.

the work of Schneider *et al.*[2]. For thermal boundary conditions, they imposed adiabatic sidewalls "while the top and bottom surfaces where maintained at time-varying hot and cold temperatures."

Since the transport phenomena in DS solidification can be dominated by thermosolutal convection, this series of simulations was undertaken to see whether the entire length of the overlying liquid should be included in the computational domain of computer simulations if one wishes to capture the interaction between the convecting liquid and the advancing solid. Tewari and Shah[1] reported macrosegregation along the lengths of small diameter (7 mm) rods of Pb-Sn alloys (10 to 58 wt. % Sn) when they were directionally solidified in strong positive thermal gradients (melt on top, solid below, and gravity pointing downwards). The results presented here are numerical simulations of the convection and segregation in directionally solidified Pb-23.2 wt. % Sn alloy, using the thermal conditions specified by Tewari and Shah.

With a finite element simulator, the solidification process is modelled by solving the fully coupled equations of momentum, energy, and solute transport, along with the constraint of assuming local equilibrium on the complex solid-liquid interface in the mushy zone. The simulations are based on a mathematical model[3-6] of dendritic solidification, in which the mushy zone is treated as an anisotropic porous medium of variable porosity. At each node the simulator solves for temperature, the fraction of liquid, the velocity components, the concentration of Sn in the liquid, and the microsegregated concentration of Sn in the solid. Furthermore, when selecting a mesh for effecting accurate calculations relevant length scales are the primary dendrite arm spacing and the thickness of a solutal boundary layer at the top of the mushy zone. This leads to a very fine mesh; *e.g.*, Huang *et al.*[7] used a two dimensional mesh with elements that were only 175 μm wide by 500 μm tall, and Schneider *et al.*[2] used a mesh with elements that were only 1 mm by 2 mm. In order to run simulations, past efforts have been restricted to relatively small domains because of the computational requirements.

RECEIVED
OCT 16 2003
OSTI

The reason for using a small container size might not be obvious to many in industry who use commercial codes in their day to day practice. Indeed, producers of turbine blades are able to obtain results of simulations with hundreds of thousands or more of elements, showing the production of an entire casting tree[8]. However, simulations such as these rarely solve for more than the temperature field. When one considers simulations of solidification with thermosolutal convection, such as those produced by Felicelli *et al.*[9] and Schneider *et al.*[2] which require the solution of two velocity components, the concentration of each alloy element in both the solid and the liquid, the temperature, and the fraction liquid at each node, it becomes apparent why small domains are used.

Although computational costs continue to go down, for those interested in thermosolutal convection it will be some time before they become reasonably affordable. It, therefore, becomes important to assess what effect domain size might have on the calculated results. By conducting four simulations of directional solidification, this study indicates that one need not simulate the entire domain to predict whether a severe form of macrosegregation known as freckling will occur, but in order to model the thermosolutal convection of the liquid above the mushy zone the full height of the overlying liquid should be included.

II. MODEL SUMMARY

Details of the model used in this study may be found elsewhere[4]. Briefly stated the finite element method is used to solve a continuum model. The model is based on a set of equations that comprises conservation of mass, conservation of energy and the concentration of solute, and the component momentum equations. Furthermore, the mushy zone is treated as a porous medium of variable volume fraction liquid, which varies from zero (all-solid region) to one (all-liquid region). When the volume fraction of liquid is zero, the set of equations reduces to the energy equation and when the volume fraction of the liquid is one the system becomes the Navier-Stokes equations for momentum and the usual advective and diffusive forms of the energy and solute

conservation equations for single phase fluids. Thermodynamic and transport properties used in the simulations are given in Table I.

As mentioned above, four computational domain sizes, from 0.05 m to 0.20 m tall, were considered. For verification purposes the width, withdrawal rate, and thermal conditions were modeled after "Case 3c" from Tewari and Shah[1], a case with freckles along the side wall. This case corresponds to a directionally solidified, 7 mm diameter, Pb-23.2 wt. % Sn casting made in a Bridgeman-type furnace. The starting condition for this sample was a 5 cm long solid of the same alloy in contact with a liquid column of about 20 cm. The quartz enclosed specimen was then directionally solidified at a rate (V) of 6 $\mu m \cdot s^{-1}$ for 0.127 m and quenched, with furnace conditions producing a thermal profile similar to the one shown in Figure 1. Since the furnace was translated at a constant rate, the temperature profile of Fig. 1 was transformed to temperature versus time for the vertical coordinates along the length of the specimen. Also the diameter of the specimen was only 7 mm so there was no radial temperature variation. Hence, we used the transformed temperatures as the thermal boundary conditions in the form of temperature versus time at nodal coordinates along the vertical surface of the computational domain. Also shown in Figure 1 is a broken line, which represents a constant thermal gradient in the liquid. This is discussed in a different section of this article.

Although Tewari and Shah[1] solidified alloys in the form of circular cylinders, our simulations are in two-dimensional rectangular domains of width 7 mm. We accept that the simulations do not capture the full three-dimensional convection patterns in the experimental alloys (*e.g.*, see Felicelli *et al.*[15]). Our calculated results, however, are robust enough to show channels located at the surface of the casting walls and segregated internal pockets in the mushy zone of the solidifying alloy, in agreement with the observation of freckles in the experimental casting. Simulated results at different times show the unsteady nature of the convection cells and the development of the channels in the mushy zone.

The primary dendrite arm spacing used in the simulations was 185 μm taken from the experiment of Tewari and Shah[1]. With dendritic columnar grains, the permeability is anisotropic with components K_x and K_z for flow perpendicular and parallel to the columnar dendrites, respectively; K_x and K_z depend on the primary dendrite arm spacing and fraction liquid. Both side walls are thermally insulated, and the bottom surface and the two side walls are impermeable to all mass and solute fluxes. The top surface ($z = H$) is treated as a surface with the normal velocity component set at zero.

A summary of the domain sizes investigated and how these domains were meshed appears in Table II. In each case the mesh was established by requiring the element to be smaller in the x-direction than the dendrite arm spacing and smaller in the y-direction than D/V. Simulations were run until the liquidus isotherm had progressed approximately 72 % of the way up the computational domain, resulting in data sets that captured between 6000 to 24 000 s of solidification information.

III. RESULTS AND DISCUSSION

First, it is instructive to view results at a particular time step. Figure 2 is a plot of temperature versus distance from the bottom of the specimen. The arrows indicate the heights of the four domains for the simulations. Also shown are the liquidus temperature (546 K) and eutectic temperature (456 K) of the alloy. In the four cases, there is a completely developed mushy zone. The overlying liquid, when the total height is set at 50 mm, is about 15 mm, and the thermal gradient in the overlying liquid is approximately uniform. When the total height is set at 100, 150 and 200 mm the overlying liquid extends further into the hot zone, where the temperature is almost uniform. Figure 3 describes how the composition of the overlying liquid depends on the domain size. Within this figure, the regions labeled "L+S" are the mushy zones. From this figure it becomes apparent that as domain size increases the overlying liquid becomes more dilute. In a lead-tin alloy, Sn is rejected into the liquid as solidification progresses. Within the mushy zone there is a negative concentration gradient from the eutectic isotherm to the leading front of the mushy zone (*i.e.*, the dendrite tips). Because the solute (Sn) is less dense than the solvent (Pb) this negative concentration gradient results in a destabilizing

liquid density profile that is cause for thermosolutal convection. Indeed, by looking at Figure 3(d) one sees solute rich plumes emanating from the mushy zone. Although the plumes are less obvious in Figures 3(b) and 3(c) and not seen in Figure 3(a) (because of how the plots are scaled), plumes such as the ones seen in Figure 3(d) enrich the overlying liquid in each case. Therefore, the degree to which the overlying liquid is enriched is mainly a function of how much liquid overlies the mushy zone.

As the mushy zone advanced to the levels shown in Fig. 3, the amount of Sn transported from the mushy zone into the overlying liquid was estimated as $(\overline{C} - C_o)H_tW$, where $\overline{C}$ is the average concentration of Sn in the liquid, C_o is original concentration of Sn, and H_t and W are the total height and width of the liquid, respectively. The amount of Sn transported into the liquid is approximately the same in Figures 3(b), (c) and (d) and about 40 pct more than in Figure 3(a). Hence, the strength of the thermosolutal convection in the overlying liquid of Figure 3(a) is significantly less than that in Figures 3(b), (c) and (d).

Figure 4 shows how the convective activity, as measured by the maximum velocity, increases as the domain size gets bigger. In order to determine why convection increases as the domain size gets taller one must determine how the compositional differences noted above alter the buoyancy forces in the system. This tact was used by Schneider *et al.*[2] to explain why the velocities changed from 1 $mm \cdot s^{-1}$ to 7 $mm \cdot s^{-1}$ for different systems considered. However, in their case the higher velocities were attributed to "stronger solutal buoyancy forces" that arose when the initial composition of their nickel-base system was changed by simultaneously decreasing tantalum ($k < 1.0$) and increasing tungsten ($k > 1.0$).

The effect of the composition of the liquid on the buoyancy forces may be ascertained from Figure 5. This figure shows plots that correspond to the liquid density for each of the cases. The plots were made by scanning along the centerline of each domain, from the bottom of the mushy zone to the top of the domain. The density of the liquid is calculated by:

$$\rho = \rho_0[1 - \beta_T(T - T_0) - \beta_C(C_l - C_0)] \quad (1)$$

Equation 1 shows that density is a linear function of temperature, T, and the solute concentration, C_l, where β_T is the thermal expansion coefficient (0.000116 K^{-1}) and β_c is the solutal expansion coefficient (0.0049 wt. $\%^{-1}$). For the reference state, the concentration is that of the initial melt (C_0) and the reference temperature (T_0) is the liquidus temperature corresponding to C_0.

Since the temperature is the same in all four simulations (Fig. 2), then the overall shapes of the curves depend mainly on the temperature field and are similar but the differences of the densities in the overlying liquid are attributed to the differences in solute content. One may view the plots as having three distinct regions in the overlying liquid. The first, between 0.035 m and 0.05 m, corresponds to the steepest density gradient in the liquid; the second, between 0.05 m and 0.09 m, corresponds to a region of decreasing density gradient; and the third to a region of almost zero density gradient. As the casting size increases so does the length of the third region in the plots.

As can be seen in Figure 5, as the domain size gets larger the plots of density in the overlying liquid are shifted toward the right, a shift that represents a move to a more dense overlying liquid. Of course, this shift is a response to the fact that the concentration of Sn in the overlying liquid is less as the domain size gets larger. Although in each case, a liquid with a stabilizing density gradient sits on top of the mushy zone, it must be remembered that it is the solute rich liquid rejected from the mushy zone that drives the thermosolutal convection.

Table III summarizes the characteristics of the liquid inside the channels of each case at the exact same location that corresponds to a point near the right vertical boundary and just below the dendrite tips. Looking at Table 3 it becomes immediately apparent that, indeed, the liquid inside the channels is obviously enriched with solute, and its density is less than density of the overlying liquid in the region just above the top of the solidification front. This is important because this difference in density is the driving

force for convection, and the differences become only slightly greater as the computational domain gets larger, as seen in Fig. 5.

Figure 6 describes the composition of the overlying liquid for the 0.05, 0.10, 0.15, and 0.20 m cases at 6000, 12 000, 18 000, and 24 000 s, respectively. The overlying liquid represents approximately 28 % of the domain in each case. Consequently, the fully solidified region for the simulation of the domain of height 0.2 m at 24 000 s is much larger than it is for the 0.05 m case at 6000 s, and the overlying liquid is more highly enriched and therefore less dense for the taller cases. The maximum velocities are also noted in Figures 6(a), (b), (c) and (d), and they increase in the order of the height of the overlying liquid.

To explain the dependence of the strength of the convection on the height of the overlying liquid, we start with the vertical component of the momentum equation:

$$\rho\left(u\frac{\partial v}{\partial x}+v\frac{\partial v}{\partial y}\right)=-\frac{\partial p}{\partial y}+\eta\left(\frac{\partial^2 v}{\partial x^2}+\frac{\partial^2 v}{\partial y^2}\right)-\rho g \qquad (2)$$

where ρ is the density, η is the viscosity, x and y are the horizontal and vertical coordinates, u and v are the x-directed and y-directed velocity components, P is pressure, and g is the gravitational acceleration (positive y-direction is upward). Since the solidification rate is only 6 μmAs^{-1}, we ignore the transient term on the left side of Eq. (2) but maintain the inertial terms. In buoyancy-driven flows of the type seen in Figs. 4(b), (c) and (d) with strong inertial effects, the buoyant forces are balanced mostly by inertial forces. Hence, if we go through a scaling procedure that is presented in Dantzig and Tucker[16], then it can be shown that the velocity scales as

$$V=\sqrt{\left(\frac{\overline{\rho}-\rho}{\rho}\right)gH_t} \qquad (3)$$

where H_t is the total height of the overlying liquid and $\overline{\rho}$ is either an average density or a reference density.

Taking the relative density change to be approximately the same in the seven simulations of Figures 3 and 6, then Eq. (3) reduces to $V \propto \sqrt{H_t}$. The maximum velocities are plotted against $H_t^{1/2}$ in Fig. 7, where it can be seen that the proportionality is followed approximately. A linear regression of the seven points in Fig. 7 gives an intercept of only 0.119 mm·s^{-1}, but Eq. (3) predicts zero. Nevertheless, within the accuracy of a scaling analysis we see that the strength of the convection in the overlying liquid relates to the square root of total height of the liquid.

An issue of practical relevance is how the domain size affects the macrosegregation in the system. Figure 8 shows plots taken from the output at 6000 s and z = 0.02 m, which is within the completely solid zone. One plot is from the simulation of the domain of height 0.05 m, and the other is from a domain of height 0.20 m. The macrosegregation is similar; the highly enriched regions along the side walls are freckles which are the deleterious effects of the channels discussed above. The solute-depleted region next to the wall channels is produced by suction of solute by the channels, as explained in Ref. [3]. The smaller peaks next to the depleted region are most probably due to the difficulty for the numerical scheme in capturing the particularly narrow channels of this simulation. A calculation made with a finer mesh in the horizontal direction reduced the magnitude of the peaks, supporting this hypothesis.

Another consideration is whether the temperature in the overlying liquid can be assumed to be in a constant gradient. We compare the previous results of the domain with a height of 5 cm to the same with the assumption that the gradient is constant (115 K/cm), shown by the broken line in Figure 1. The magnitudes of the velocities at 3000 s are shown in Figure 9. When a constant gradient is assumed (Figure 9(b)), the magnitude of the velocity in the overlying liquid is somewhat less than when the unmodified temperature is used. At 3000 s, the unmodified thermal gradient varies from a maximum of about 114 K just above the dendrite tips to only 28 K at the top of the domain. Taken by themselves, both cases present a liquid with a stabilizing thermal gradient, so the case of a high and constant gradient has the smaller maximum velocity, albeit the effect is not profound. A third case of a constant gradient set at 69 K/cm (not shown) had a maximum

magnitude intermediate between the cases of Figures 9(a) and 9(b), which is in-line with this reasoning.

The effect of assuming a constant thermal gradient on the segregation in the fully solidified alloy is very slight, as shown in Figure 10. The concentrations of Sn in the freckles at the vertical surfaces is about 37 wt. % in both cases, and the concentrations across both castings are practically equal.

IV. CONCLUSIONS

Our ability to model the convective transport in the overlying liquid depends upon the height of the liquid that we choose to include in the computational domain. In the cases studied herein, we found that the strength of the convection in the overlying liquid depends on the square root of the height of the liquid. Perhaps a more important conclusion of this work is that one need not model the entire domain to predict a particularly severe form of macrosegregation known as freckling. While macrosegregation and convection were found to change to varying degrees when the computational domain height was changed, the ability to predict freckles was not impacted. In recognizing this, one might be able to employ a model such as the continuum model used here in a practical situation where freckles are of concern. For example, because of time constraints, producers of critical components such as directionally solidified single crystal turbine blades rarely solve for more than the temperature field in simulations even though the capability to predict freckles could go a long way in reducing defects. This study suggests that it would be feasible to use data produced by commercial codes used already—in the form of temperature histories—on critical sections of the casting without losing the ability to predict whether freckles will result. It was also shown that assuming a constant thermal gradient in the liquid causes the convection in the overlying liquid to be somewhat weaker than the convection in the actual temperature distribution. The segregation in the completely solidified casting, however, is hardly affected by assuming that the gradient is constant.

ACKNOWLEDGMENTS

This work was partially supported by the United States Department of Energy under Contract No. DE-AC04-94AL85000. Sandia National Laboratories is a multiprogram laboratory operated by Sandia Corporation, a Lockheed Martin Company, for the Uniteds States Department of Energy. One of the authors (CF) appretiates the support of Sandia's Materials and Proecesses Center. DRP and SDF appreciate the support provided by the Division of International Programs of the National Science Foundation (United States) and by Consejo National de Investigaciones Cientificas y Tecnicas (Argentina), under the frame of the international cooperation project, "Simulation of Defects in Castings." The authors appreciate the assistance of S.N. Tewari, Clevland State University (Cleveland, OH), who provided experimental conditions that were used in our simulations, and or many discussions with P.K. Sung and J.C. Heinrich, The University of Arizona (Tucson, AZ). SDF appreciates the grant provided by Argencia Nacional de Promocion Cientificas y Tecnologica (PICT98 12-03239).

REFERENCES

1. S. N. Tewari and R. Shah: *Metall. Trans. A*, 1992, vol. 23A, pp. 3383-92.
2. M. C. Schneider, J. P. Gu, C. Beckermann, W. J. Boettinger, and U. R. Kattner: *Metall. Mater. Trans. A*, 1997, vol. 28A, pp. 1517-31.
3. S. D. Felicelli, J. C. Heinrich and D. R. Poirier: *Metall. Trans. B*, 1991, vol. 22B, pp. 847-59.
4. S. D. Felicelli, J.C. Heinrich, and D.R. Poirier: *Num. Heat Transfer, Part B*, 1993, vol. 23, pp. 461-81.
5. S. Ganesan and D. R. Poirier: *Metall. Trans. B*, 1990, vol. 21B, pp. 173-81
6. D. R. Poirier, P. J. Nandapurkar and S. Ganesan: *Metall. Trans. B*, 1991, vol. 22B, pp. 889-900.
7. H. W. Huang, J. C. Heinrich and D. R. Poirier: *Modelling Simul. Mater. Sci. Eng.*, 1996, vol. 4, pp. 245-59.
8. J. S. Tu, R. K. Foran, A. M. Hines, and P. R. Aimone, *JOM*, 1995, vol. 47 (10), pp. 64-8.
9. S. D. Felicelli, J. C. Heinrich, and D. R. Poirier: *Inter. J. Numer. Meth. Fluids*, 1998, vol. 27, pp. 207-27.
10. *Smithells Metals Reference Book*, 7th ed., E. A. Brandes and G. B. Brook, eds., Butterworth-Heineman, Oxford, 1992, p. 11-421.
11. D. R. Poirier: *Metal. Trans. A*, 1988, vol. 19A, pp. 2349-54.
12. H. R. Thresh and A. F. Crawley: *Metall. Trans.*, 1970, vol. 1, pp. 1531-5.
13. D. R. Poirier and P. Nandapurkar: *Metall. Trans. A*, 1988, vol. 19A, pp. 3057-61.
14. J. R. Sarazin and A. Hellawell: *Metall. Trans. A*, 1988, vol. 19A, pp. 1861-71.
15. S. D. Felicelli, J.C. Heinrich and D.R. Poirier: *J. Cryst. Growth*, 1998, vol. 191, pp. 879-88.
16. J. A. Dantzig and C. L. Tucker III, *Introduction to Modeling of Materials Processing*, Campus Publishing Services, Urbana, IL, 1998, pp. 172-76.

Table I. Thermodynamic and transport properties used for calculations in Pb-23.2 Wt. % Sn

Property	Reference
Reference concentration (C_0), 23.2 wt. % Sn	—
Reference temperature (T_0), 545.94 K	[10]
Equilibrium partition ratio (k), 0.31	[10]
Melting point of lead, 600 K	[10]
Slope of liquidus, -2.33 K · (wt. %)$^{-1}$	[10]
Density [$\rho_0 = \rho(C_0,T_0)$], 9.53 x 10^3 kg · m^{-3}	[11]
Thermal expansion coefficient (β_T), 1.16 x 10^{-4} K^{-1}	[11]
Solutal expansion coefficient (β_C), 4.9 x 10^{-3} (wt. %)$^{-1}$	[11]
Kinematic viscosity, 2.62 x 10^{-7} m^2 · s^{-1}	[11, 12]
Latent heat, 39.78 kJ · kg^{-1}	[13]
Specific heat of solid, 0.176 kJ · kg^{-1} · K^{-1}	[13]
Average thermal conductivity, 0.0206 kW · m^{-1} · K^{-1}	[6]
Thermal diffusivity, 1.17 x 10^{-5} m^2 · s^{-1}	[11, 13, 6]
Solutal diffusivity (D), 3 x 10^{-9} m^2 · s^{-1}	[14]

Table II. General information regarding the simulations

Height (m)	Width (m)	Mesh Spacing	Total time simulated (s)
0.05	0.007	115 x 40	6000
0.10	0.007	225 x 40	12 000
0.15	0.007	340 x 40	18 000
0.20	0.007	450 x 40	24 000

Table III. Data obtained from within the channels at coordinates: $x = 0.0069$ m, $y = 0.034$ m and $t = 6000$ s

Domain Height (m)	ρ_l (kg · m^{-3})	C_l (wt. % Sn)
0.05	9158	31.48
0.10	9163	31.38
0.15	9152	31.61
0.20	9156	31.53

FIGURE CAPTIONS

Fig. 1 - Thermal profile similar to the one given by Tewari and Shah [1]. The broken line is an extrapolation of temperature for a uniform gradient of 115 K/cm in the overlying liquid. T_0 and T_E are the liquidus and eutectic temperature, respectively.

Fig. 2 - Temperature distributions in the DS-specimens with total heights of the computational domain set at 50, 100, 150 and 200 mm (indicated by the arrows). T_0 and T_E indicate the liquidus and eutectic temperatures, respectively.

Fig. 3 - Liquid concentration of wt. pct Sn at 6000 s: (a) 0.05 m tall, (b) 0.10 m tall, (c) 0.15 m tall, (d) 0.20 m tall. The average concentrations of Sn in the overlying liquid are (a) 27.5 pct, (b) 24.77 pct, (c) 24.21 pct, and (d) 23.92 pct.

Fig. 4 - Magnitude of the velocities ($mm \cdot s^{-1}$) at 6000 s: (a) 0.05 m tall, (b) 0.10 m tall, (c) 0.15 m tall, (d) 0.20 m tall. The "L+S" region defines the mushy zone in each case. The maximum magnitudes are (a) 1.02 $mm \cdot s^{-1}$, (b) 2.00 $mm \cdot s^{-1}$, (c) 3.00 $mm \cdot s^{-1}$, and (d) 3.52 $mm \cdot s^{-1}$.

Fig. 5 - Liquid density along the centerline, through the mushy zone and overlying liquid of each domain at 6000 s.

Fig. 6 - Liquid concentration of wt. % Sn at (a) 6000 s, (b) 12 000 s, (c) 18 000 s, (d) 24 000 s for 0.05, 0.10, and 0.15, and 0.20 m cases, respectively. The maximum velocities are (a) 1.02 $mm \cdot s^{-1}$, (b) 1.82 $mm \cdot s^{-1}$, (c) 1.94 $mm \cdot s^{-1}$, and (d) 2.11 $mm \cdot s^{-1}$.

Fig. 7 - Maximum value of the velocity in the overlying liquid versus the height of the liquid.

Fig. 8 - Simulated macrosegregation plots at $z = 0.02$ m in the all solid region of the shortest domain (0.05 m) and the tallest (0.20 m) used in the simulations.

Fig. 9 - Magnitude of the velocities ($mm \cdot s^{-1}$) at 3000 s for 0.05 m tall domains: (a) the unmodified temperature history and (b) a constant gradient of 115 K/cm in the overlying liquid. The maximum magnitudes are (a) 1.59 $mm \cdot s^{-1}$ and (b) 1.33 $mm \cdot s^{-1}$.

Fig. 10 - Predicted macrosegregation plots taken at time = 6000 s at $y = 0.02$ m, an all-solid region.

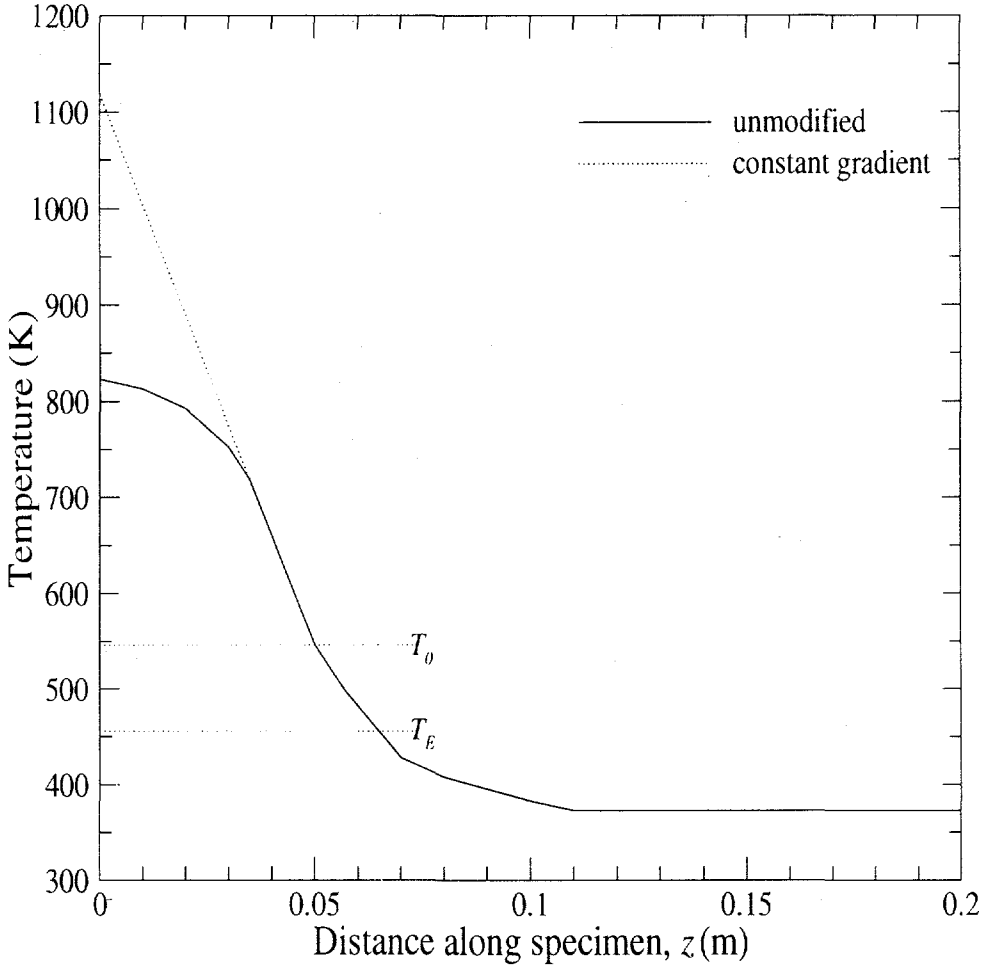

Fig. 1 - Thermal profile similar to the one given by Tewari and Shah [1]. The broken line is an extrapolation of temperature for a uniform gradient of 115 K/cm in the overlying liquid. T_0 and T_E are the liquidus and eutectic temperature, respectively.

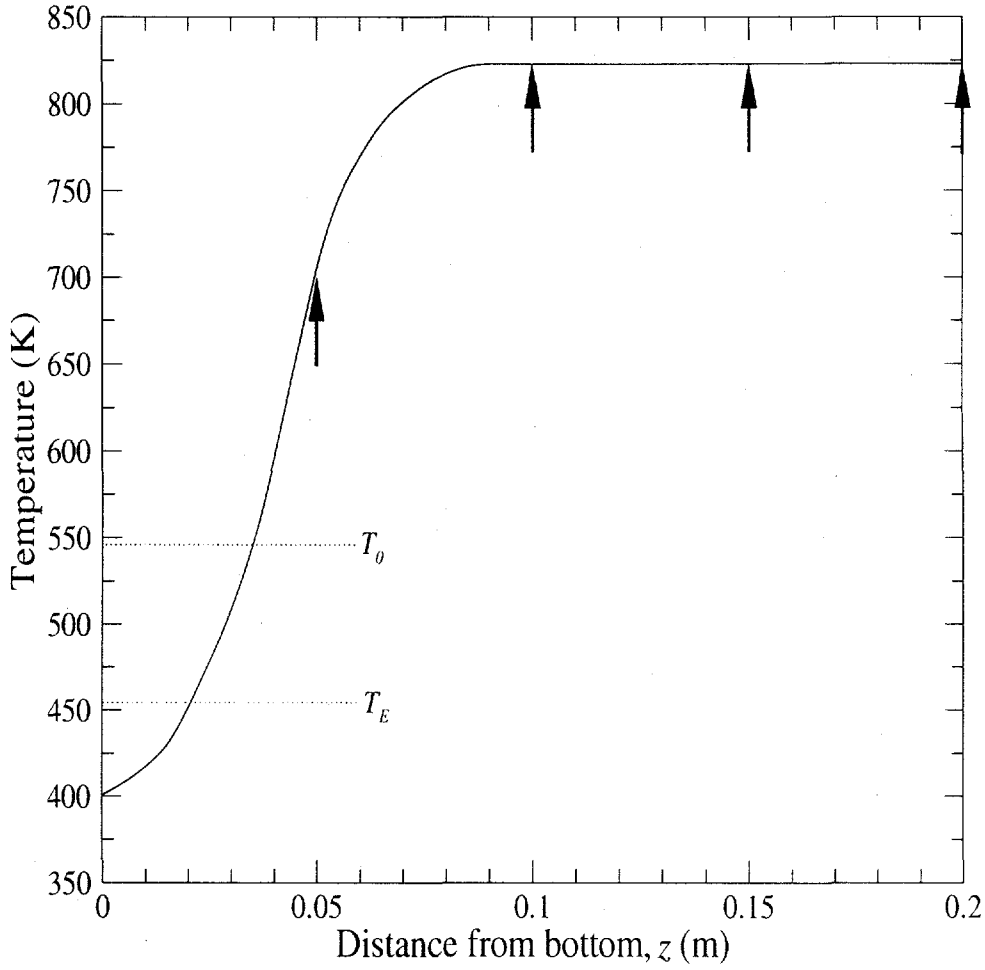

Fig. 2 - Temperature distributions in the DS-specimens with total heights of the computational domain set at 50, 100, 150 and 200 mm (indicated by the arrows). T_0 and T_E indicate the liquidus and eutectic temperatures, respectively.

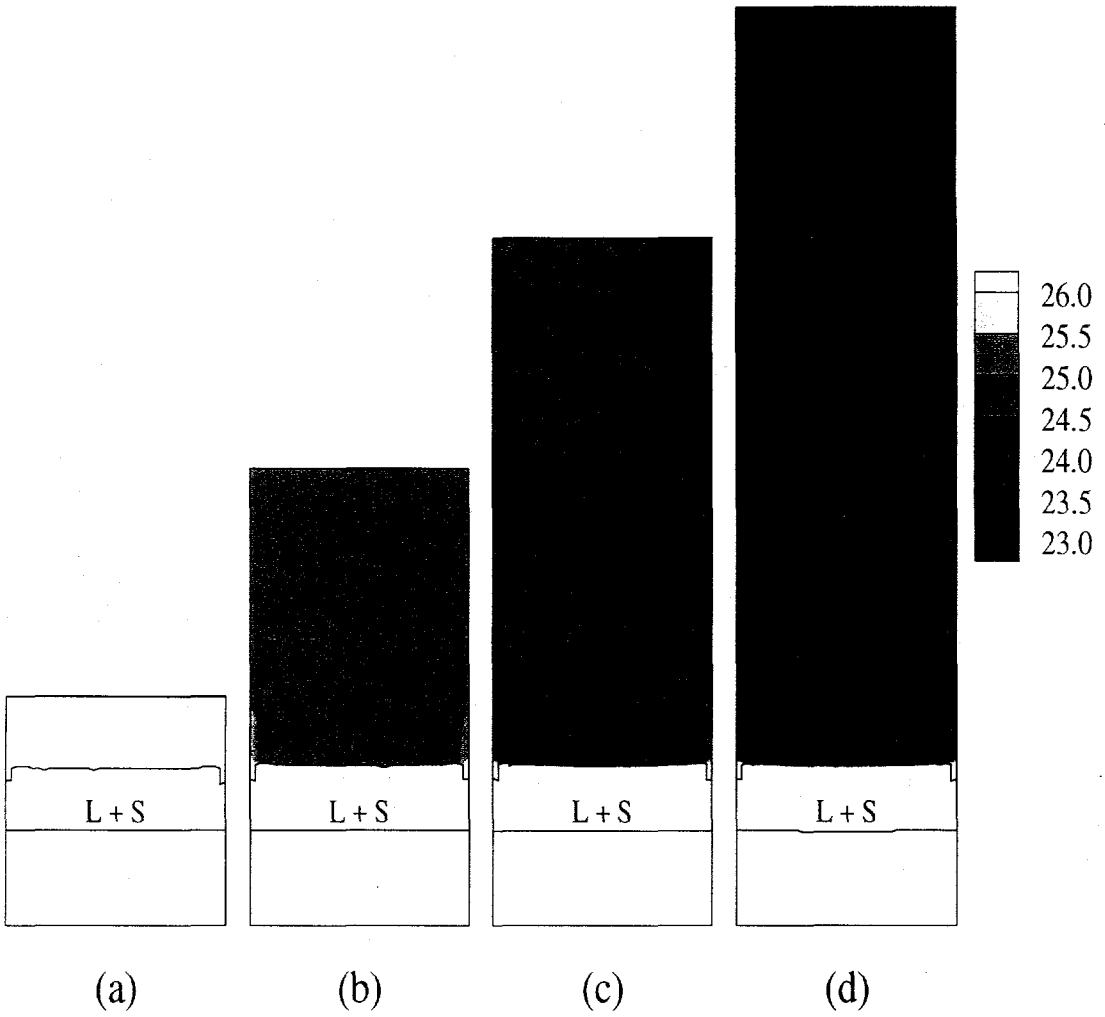

Fig. 3 - Liquid concentration of wt. pct Sn at 6000 s: (a) 0.05 m tall, (b) 0.10 m tall, (c) 0.15 m tall, (d) 0.20 m tall. The average concentrations of Sn in the overlying liquid are (a) 27.5 pct, (b) 24.77 pct, (c) 24.21 pct, and (d) 23.92 pct.

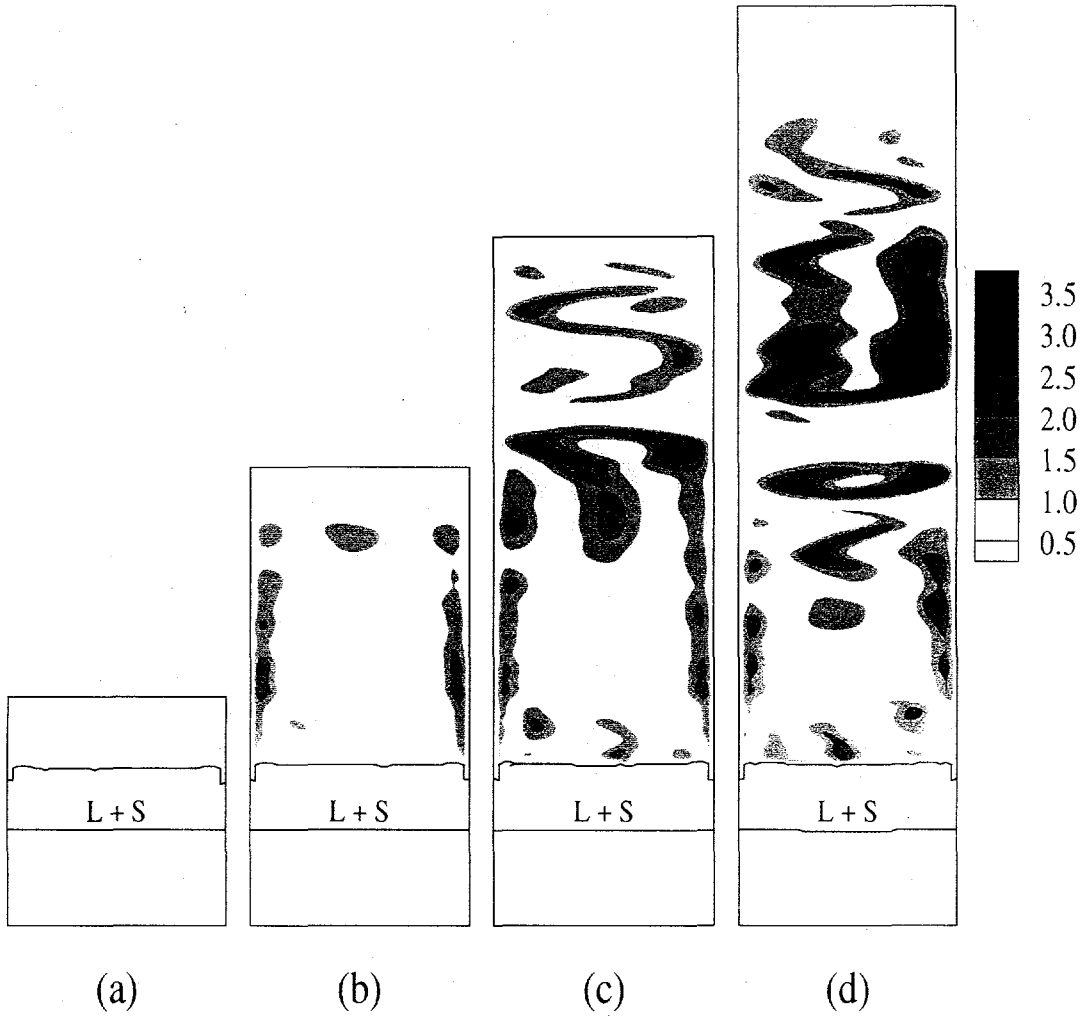

Fig. 4 - Magnitude of the velocities (mm · s^{-1}) at 6000 s: (a) 0.05 m tall, (b) 0.10 m tall, (c) 0.15 m tall, (d) 0.20 m tall. The "L+S" region defines the mushy zone in each case. The maximum magnitudes are (a) 1.02 mm · s^{-1}, (b) 2.00 mm · s^{-1}, (c) 3.00 mm · s^{-1}, and (d) 3.52 mm ·s^{-1}.

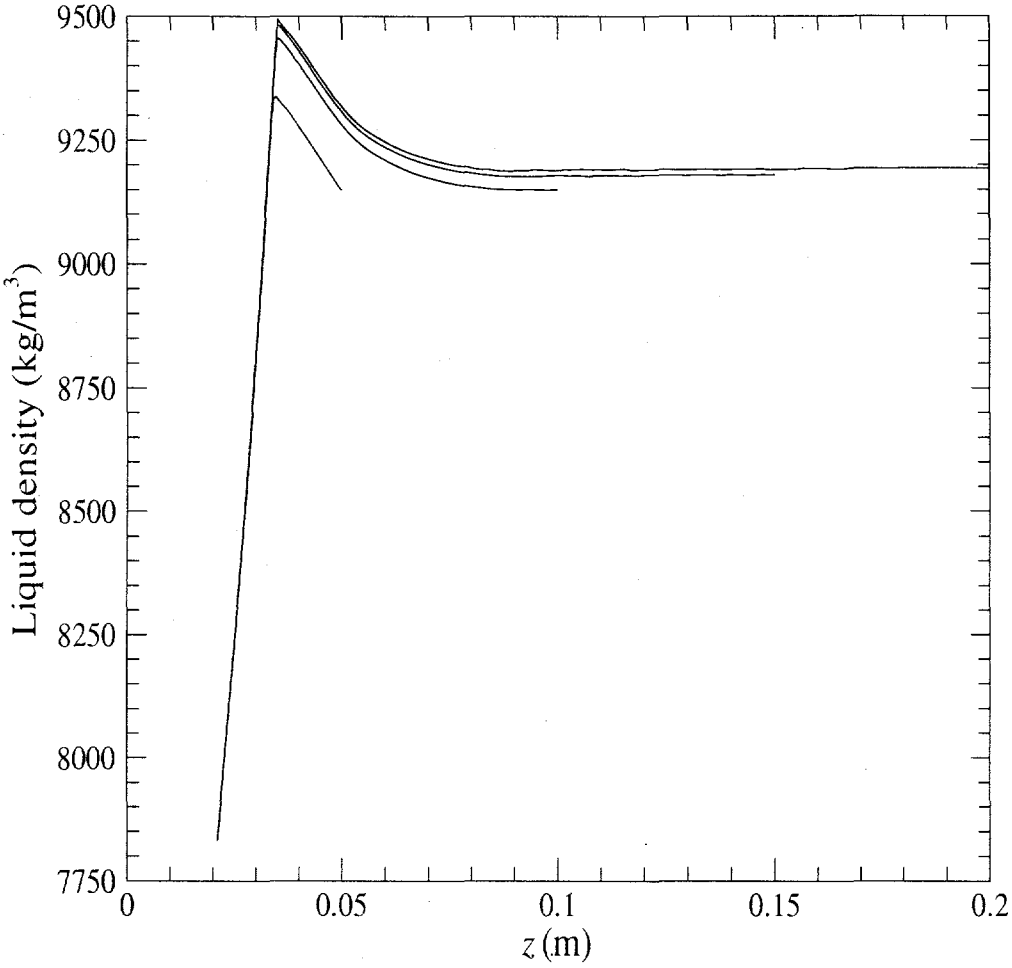

Fig. 5 - Liquid density along the centerline, through the mushy zone and overlying liquid of each domain at 6000 s.

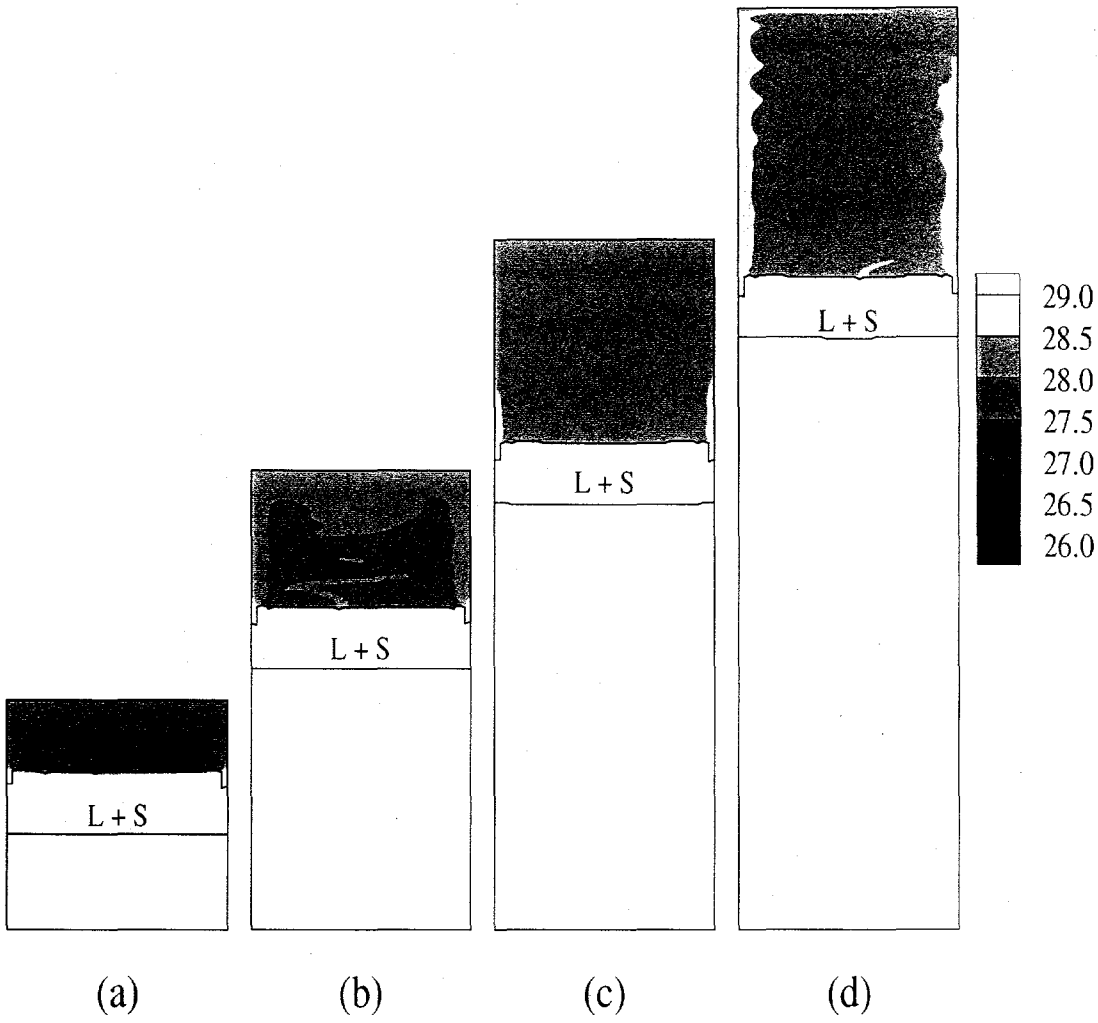

Fig. 6 - Liquid concentration of wt. % Sn at (a) 6000 s, (b) 12 000 s, (c) 18 000 s, (d) 24 000 s for 0.05, 0.10, and 0.15, and 0.20 m cases, respectively. The maximum velocities are (a) 1.02 mm $\cdot$ s^{-1}, (b) 1.82 mm $\cdot$ s^{-1}, (c) 1.94 mm $\cdot$ s^{-1}, and (d) 2.11 mm $\cdot s^{-1}$.

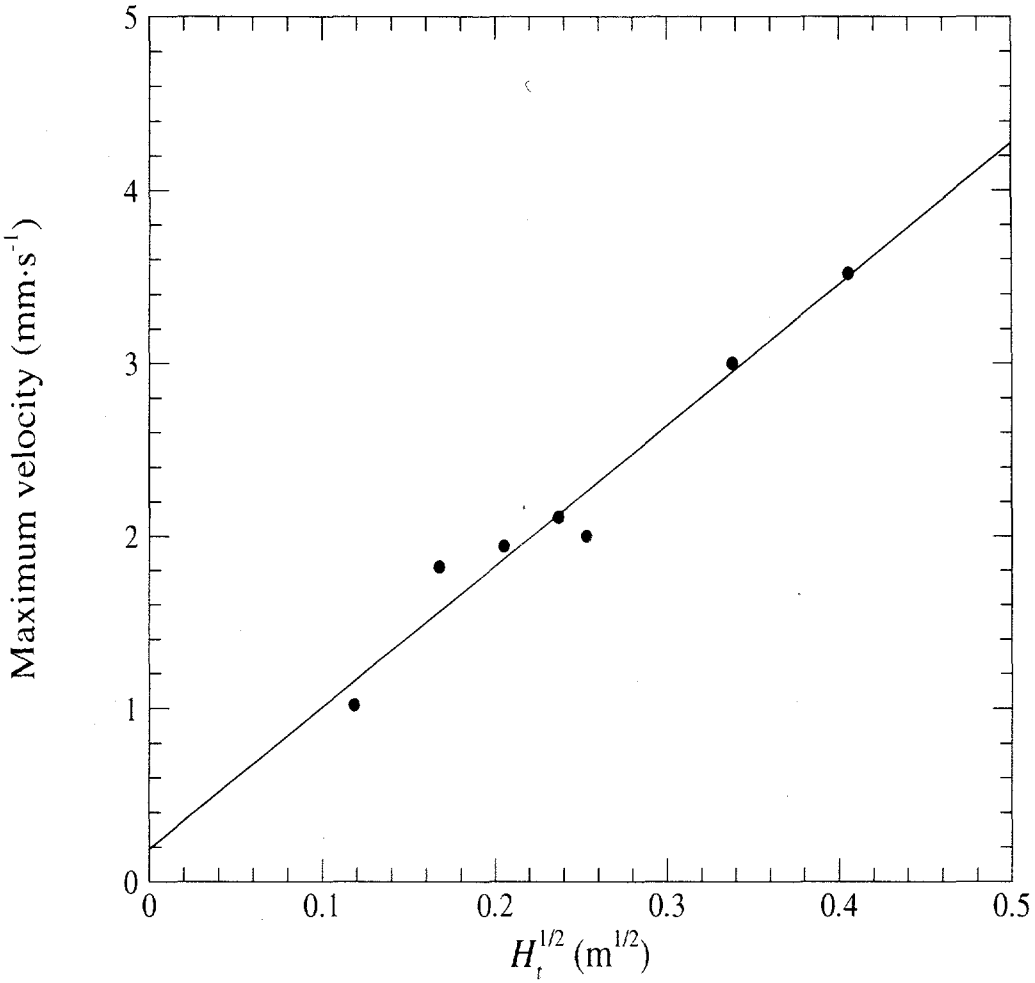

Fig. 7 - Maximum value of the velocity in the overlying liquid versus the height of the liquid.

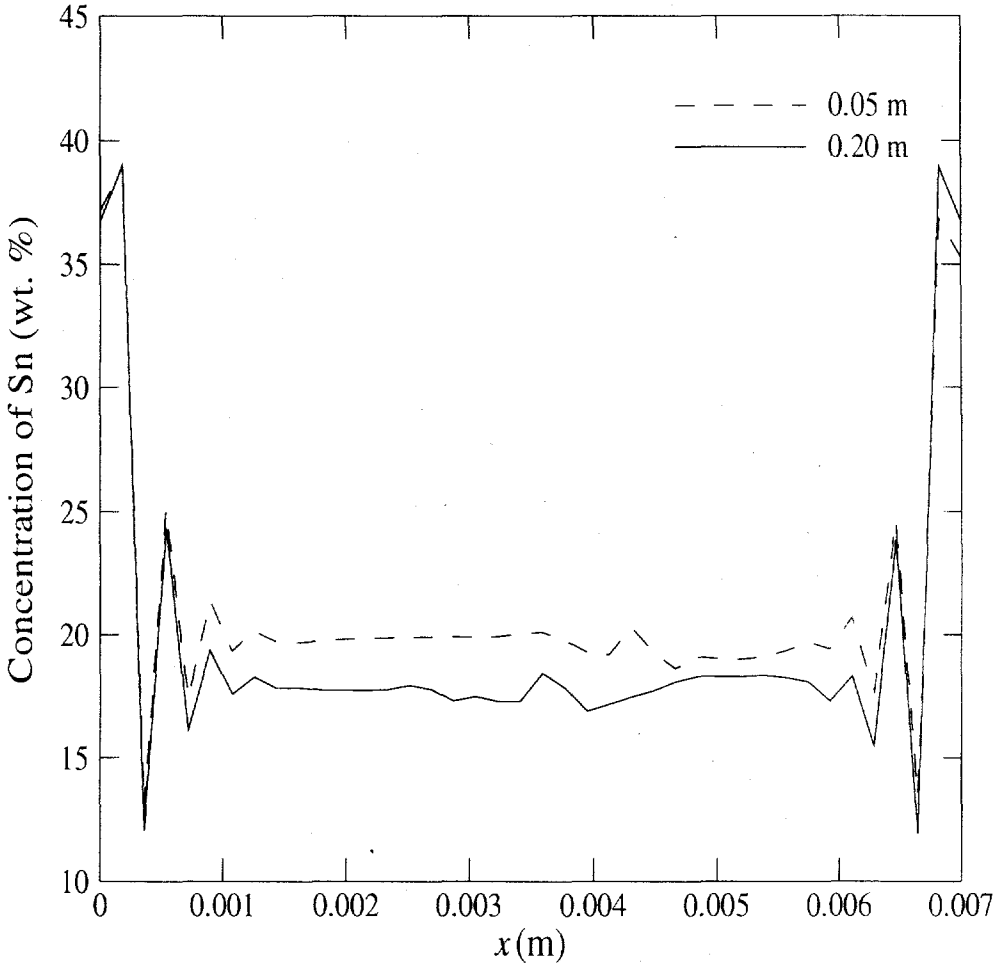

Fig. 8 - Simulated macrosegregation plots at $z = 0.02$ m in the all solid region of the shortest domain (0.05 m) and the tallest (0.20 m) used in the simulations.

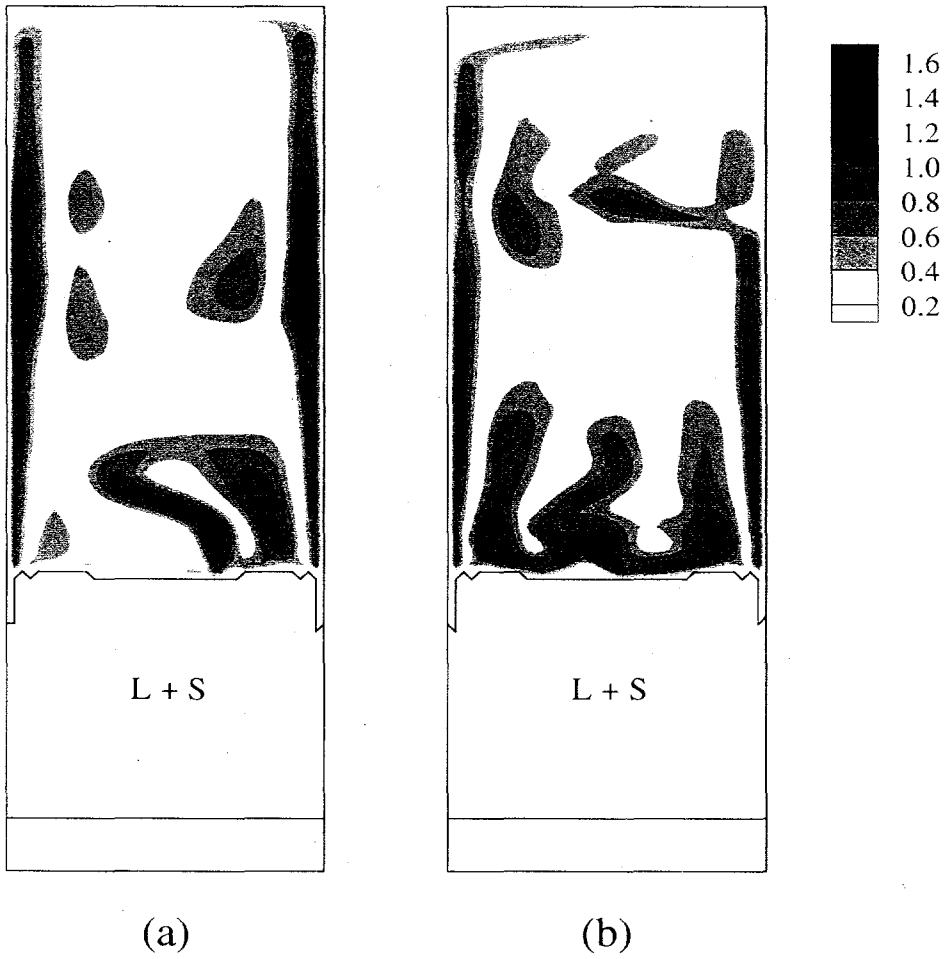

Fig. 9 - Magnitude of the velocities (mm · s^{-1}) at 3000 s for 0.05 m tall domains: (a) the unmodified temperature history and (b) a constant gradient of 115 K/cm in the overlying liquid. The maximum magnitudes are (a) 1.59 mm · s^{-1} and (b) 1.33 mm · s^{-1}.

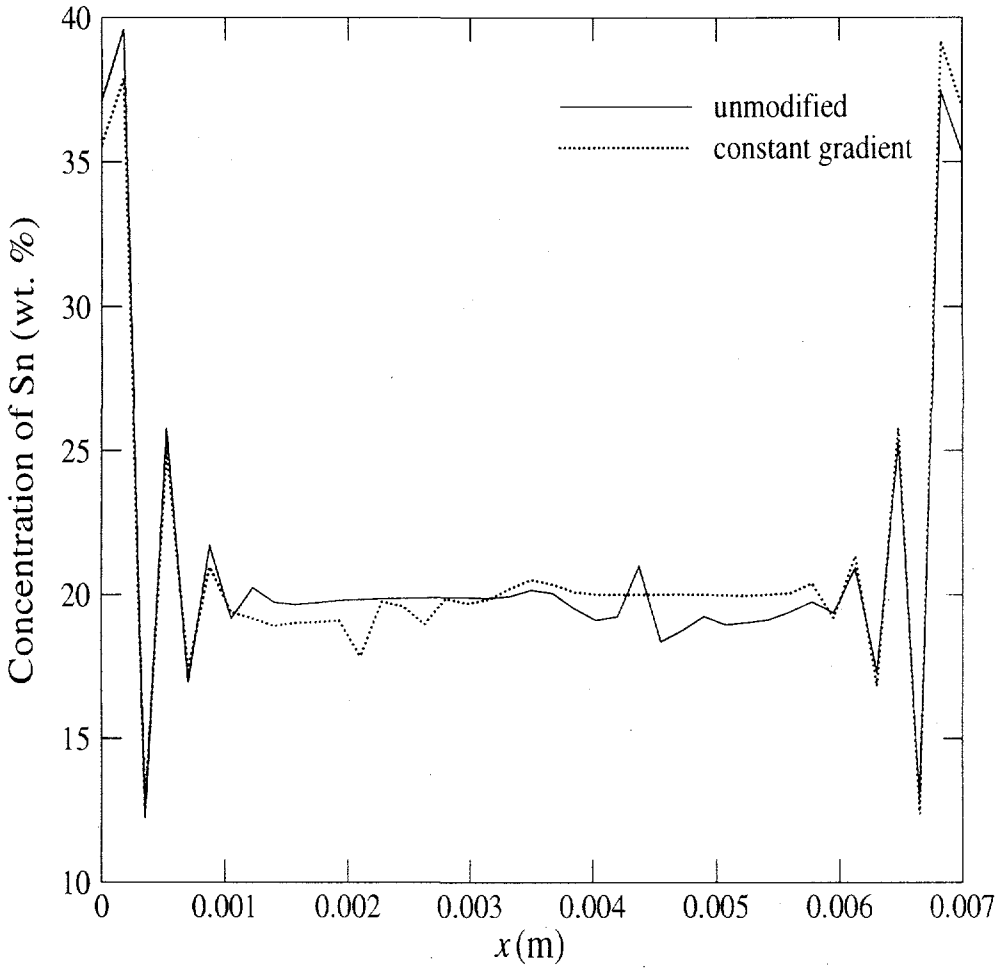

Fig. 10 - Predicted macrosegregation plots taken at time = 6000 s at $y = 0.02$ m, an all-solid region.